

Technical Memo

899

Preparing for the exploitation of MTG-S IRS in NWP using FY4-A GIIRS observations

Pierre Dussarrat (EUMETSAT) and Chris Burrows
(ECMWF)

June 2022

Series: ECMWF Technical Memoranda

A full list of ECMWF Publications can be found on our web site under:

<http://www.ecmwf.int/en/publications/>

Contact: library@ecmwf.int

© Copyright 2022

European Centre for Medium Range Weather Forecasts, Shinfield Park, Reading, RG2 9AX, UK

Literary and scientific copyrights belong to ECMWF and are reserved in all countries. The content of this document is available for use under a Creative Commons Attribution 4.0 International Public License.

See the terms at <https://creativecommons.org/licenses/by/4.0/>.

The information within this publication is given in good faith and considered to be true, but ECMWF accepts no liability for error or omission or for loss or damage arising from its use.

Abstract

The instrument GIIRS on-board FY-4A is a hyperspectral sounding instrument, it provides the first IR-sounding observations of earth's atmosphere in two large bands in the middle and long wave infrared from a geostationary orbit. Its data characteristics are very close to the future IRS instrument on-board the next generation Meteosat Third Generation sounding satellites (MTG-S), therefore both EUMETSAT and ECMWF took the opportunity to work together on a joint study in order to test their data quality analysis capabilities on “real” measurements and prepare the first assimilation of hyperspectral radiances of a geostationary instrument in a NWP model.

1 Introduction

The GIIRS instrument is an experimental Chinese Fourier transform spectrometer that flies on-board the FY-4A satellite in a geostationary orbit at around 100°E (https://space.oscar.wmo.int/satellites/view/fy_4a). It is the first thermal infrared hyperspectral interferometer on a geostationary platform and a precursor of the IRS instrument on-board the Meteosat Third Generation sounding satellites MTG-S (https://space.oscar.wmo.int/satellites/view/mtg_s1).

Each GIIRS sub-scan is composed of 128 pixels and each pixel has a footprint at NADIR of 16km. Five east-west scans (= 59 sub-scans) are realized from north to south in order to cover all Asia. The 128 pixels of each sub-scan are comprised of 4 north-south columns and 32 west-east lines, as pictured in Figure 3. The instrument records interferograms between ± 8 mm optical path distance, then a Hamming apodisation is applied and the spectra are recovered by Fourier transform. The table in Figure 1 summarises the FY-4A GIIRS characteristics in comparison to the future MTG-S IRS instrument. Both instrument characteristics are very close, therefore FY-4A provides a great opportunity to test our quality analysis tools on real measurements and prepare the first assimilation of hyperspectral radiances from a geostationary instrument in an NWP model.

Parameter	FY4A-GIIRS	MTG-IRS
Interferometer	Michelson	Michelson
Bands	700-1130cm ⁻¹ 1650-2250cm ⁻¹	680-1210cm ⁻¹ 1600-2250cm ⁻¹
Spectral sampling	0.625cm ⁻¹	-0.603cm ⁻¹
Spatial sampling (NADIR)	16km	4km
Radiometric accuracy	1.5K	0.5K
Spectral calibration	10ppm	3-1ppm
Scanning revisit	2h (China)	30min (LAC3: Europe)

Figure 1: FY4-A GIIRS instrument characteristics (www.nsmc.org.cn) compared to MTG-S IRS (www.eumetsat.int).

Indeed, the instrument FY-4A GIIRS, though being an experimental mission, offers a unique early opportunity to prepare for the assimilation of GEO-hyperspectral radiances in NWP models before the launch of MTG-S and to demonstrate with real observations the potential of MTG-S IRS for that application. GIIRS acquisitions are indeed more alike IRS at least in the temporal domain than LEO-hyperspectral sounders, which have a limited repeat cycle of 2 revisits per day, and have been the only source of real proxy-observations until GIIRS. Since the release of the GIIRS L1 products version 3 (v3) in November 2019, which includes substantial calibration improvements (Guo et al. (2021), Burrows (2020)), GIIRS

has had the potential to provide real proxy data for IRS, in systematic assimilation experiments never performed before.

In the following, we present several analyses focusing on different aspects of the GIIRS data. The first group of analyses uses collocated measurements with the IASI instruments as reference. Then, the second group entails comparison to model backgrounds. Then, a preliminary data assimilation experiment is presented.

2 GIIRS vs. IASI Analysis observation comparison

In the following sub-sections, we define collocated measurements between GIIRS and the IASI instruments on-board the Metop satellites, then we compare both the spectral and radiometric cross-calibration. All three IASI instruments perform a few flybys above Asia per day. We were able to define approximately 12000 spatio-temporal collocations during the month of September 2020. The main characteristics of the GIIRS/IASI collocation criteria are the following: the footprint distance is smaller than 7.5km, the time difference is smaller than 15min and the sounding angle difference is smaller than 20 degrees. This study revealed in particular that limiting the sounding angle difference is crucial, since it has a great impact on the measured spectra. The spatial distribution of collocations is shown in Figure 2.

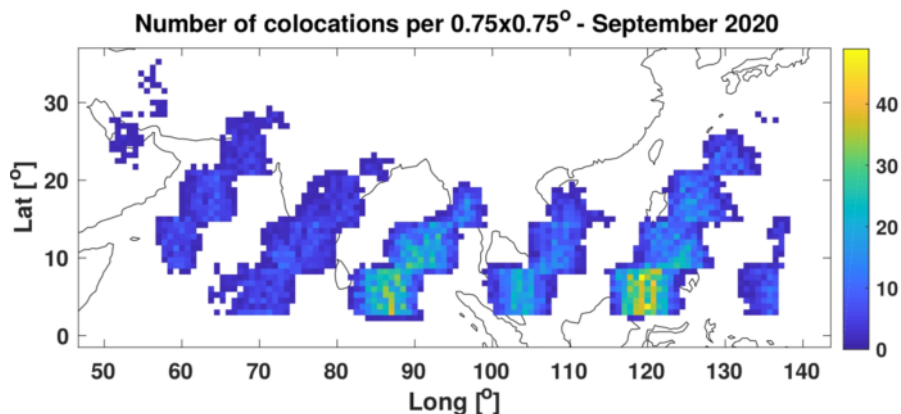


Figure 2: Number of collocation per 0.75x0.75 degrees box. It reveals a synchronisation between the IASI orbit and GIIRS scanning pattern.

2.1 Spectral Calibration

We first were able to extract the spectral calibration of GIIRS with respect to IASI, which is considered as an international reference. We looked for correlation maxima between the two measurements and computed the scaling factor $\delta v/v$ in ppm for every GIIRS pixel.

In Figure 3, the scaling factors are represented for the full detector (4x32 pixels) and then the section for the 32 pixel lines (equivalent to a north to south cut). We were able to find peculiar behaviours for both bands, in particular the calibration depends strongly on the pixel line number.

It seems that the GIIRS spectral calibration requirement of 10ppm is only partially satisfied. We were not able to conduct any time dependent analysis to pursue the investigations. Thus EUMETSAT is currently

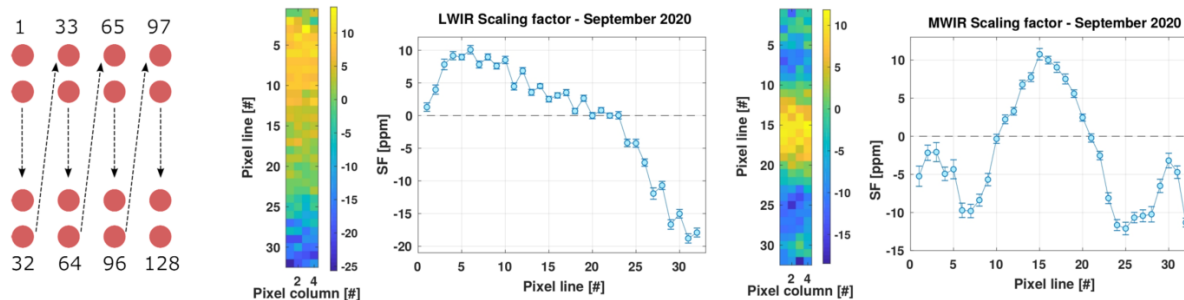


Figure 3: Numbering convention of the pixels of FY-4A GIIRS detector array into 32 lines and 4 columns (left). Spectral calibration in ppm for both bands represented for the full detector and the section along the 32 pixel lines (LWIR, middle and MWIR, right). The graphs reveal striking north-south behaviours for both bands.

developing complementary methods to access time dynamics as well in preparation of IRS.

The root of the issue is still unknown, it was previously interpreted by the team as a focal plane shift and/or defocus but to this day, after many performance simulations in the context of IRS, it seems that straylight (spurious reflections and scattering inside the instrument) could be involved.

2.2 Radiometric Calibration

We now compute the difference of radiances in equivalent temperature error at 280K for both bands. The results are presented in Figure 4 as a function of the scene type: clear (IASI cloud index < 50%), cloudy (IASI cloud index > 50%). It first revealed the evidence of a contamination inside the GIIRS instrument resulting in peaks in the difference near 720 and 1700cm^{-1} , which was already reported by the Chinese teams (Guo et al. (2021)). Then, we witness a large dependency on the scene type, the bias is positive (GIIRS measurements are colder) for clear scene and the bias is negative (GIIRS is hotter) for cloudy scenes. Moreover, we see strong spectral features remaining in the difference in the MWIR band.

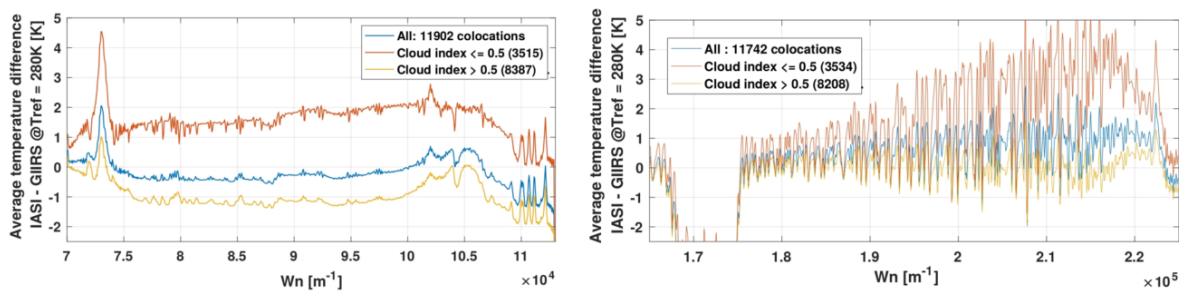


Figure 4: Radiometric calibration in K (radiance equivalent temperature at 280K) for both bands. The graphs reveal contamination lines, scene-dependent biases and spectral response function distortions for the GIIRS measurements.

Thus, it seems that the GIIRS radiometric accuracy requirement of 1.5K is only partially compliant. Concerning the scene dependency and spectral signal residuals, it appears after many performance simulations in the context of IRS that it could be related to strong straylight (spurious reflections or scattering inside the instrument). A large portion of the light is mixed inside the interferometer which leads to a

loss of thermal contrast of the spectra and a distortion of the spectral response function of all channels.

With the intention of confirming that aspect, we have examined viewing geometries at the Earth's limb. This allows a qualitative assessment of whether there is stray terrestrial radiation being measured by the pixels which should only be measuring cold space. A series of limb measurements is shown in Figure 5. When the scene covers cold space alone, the signals from all pixels are small and noise is apparent. However, as increasing amounts of terrestrial radiation enter the dwell, the measured signal in cold space increases, thus suggesting the presence of straylight contaminating the signal in cold space. This leakage between pixels will also be present in fully terrestrial scenes, but will be much harder to quantify as clean transitions in the atmosphere and surface are not uniform enough to perform such an analysis.

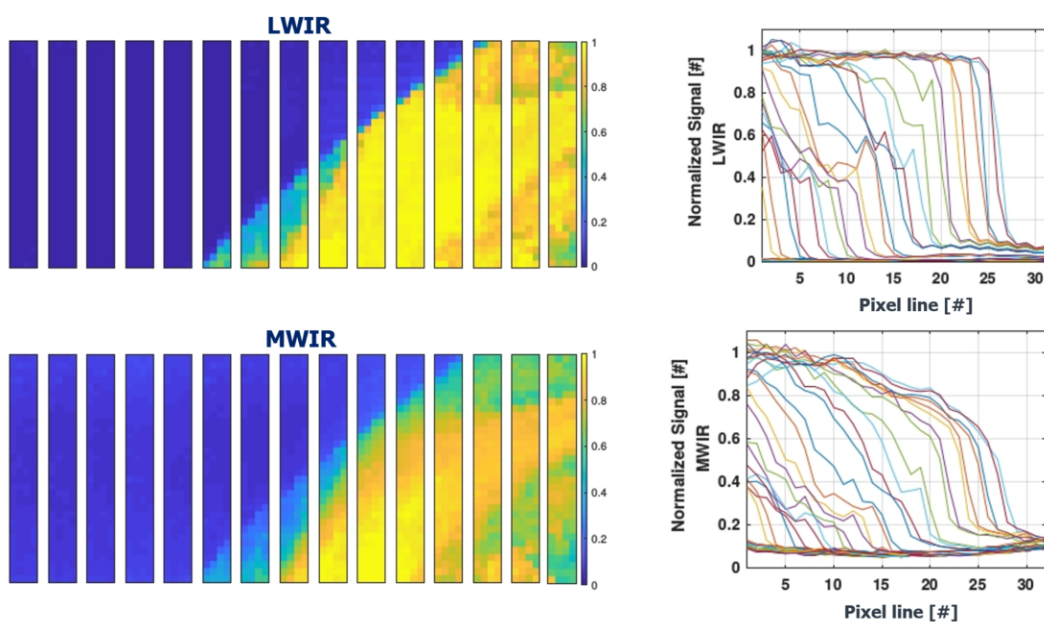


Figure 5: Several measurements are aggregated to image the earth's limb, the mean signal normalised by the image maximum value is represented for both bands (left). The associated cross sections along several detector lines are represented (right). We witness a smooth transition to space and a residual signal above the earth rim up to 20 %, particularly in MWIR, it is a hint toward straylight.

Even so, these conclusions cannot be confirmed easily without on-ground characterisation and more engineering information, it fostered our imagination and led to deeper analysis of the impact of straylight in the context of IRS to avoid this kind of behaviour in the next generation of instrument.

To conclude the analysis of collocations performed by EUMETSAT, we first confirm our capability to cross-compare LEO and GEO sounders. We reach the ppm precision for the spectral calibration and a few mK for the radiometric calibration, both are great achievements in view of the MTG-S IRS performance monitoring. Then, we revealed peculiar behaviours of the GIIRS products that hint toward strong straylight issues. Even if we cannot draw precise diagnostics for now, it developed our imagination and investigation capabilities.

3 GIIRS compared to model simulations

Comparing the observations to model simulations is complementary to comparisons with independent observations. For example, whatever the time, location and viewing angle of the observation to be compared, a simulation can be generated, using NWP model fields and a fast radiative transfer model, so a larger sample can be produced than is possible with co-locations from LEO overpasses. Furthermore, the radiative transfer model is trained on accurate line-by-line simulations, which means that in terms of assessing spectral calibration, we do not have to be concerned with any limitations in the spectral calibration of an independent observation type (although IASI has a very accurate spectral calibration).

However, using NWP simulations does have limitations. The main limitation is that currently, scenes affected by cloud cannot be simulated accurately, so for cloudy scenes, LEO co-locations are required. Furthermore, the NWP model and radiative transfer model may have deficiencies which ought to be kept in mind in judging radiometric accuracy. For this reason, the main value of comparisons with NWP model fields is not to assess absolute radiometric calibration accuracy, but to uncover any systematic inconsistencies in the data.

3.1 Radiometric Calibration

A spatial map of GIIRS observations compared to model simulations is shown in Figure 6 for a single scan of a tropospheric temperature sounding channel in the LWIR band. It is important to note that cloud is not included in the simulations, so some of the coldest regions of the domain in the observations are not reflected in the simulations. It can be seen, however, that for this channel, there is broad agreement between the observations and simulations for the warmer, clear-sky regions.

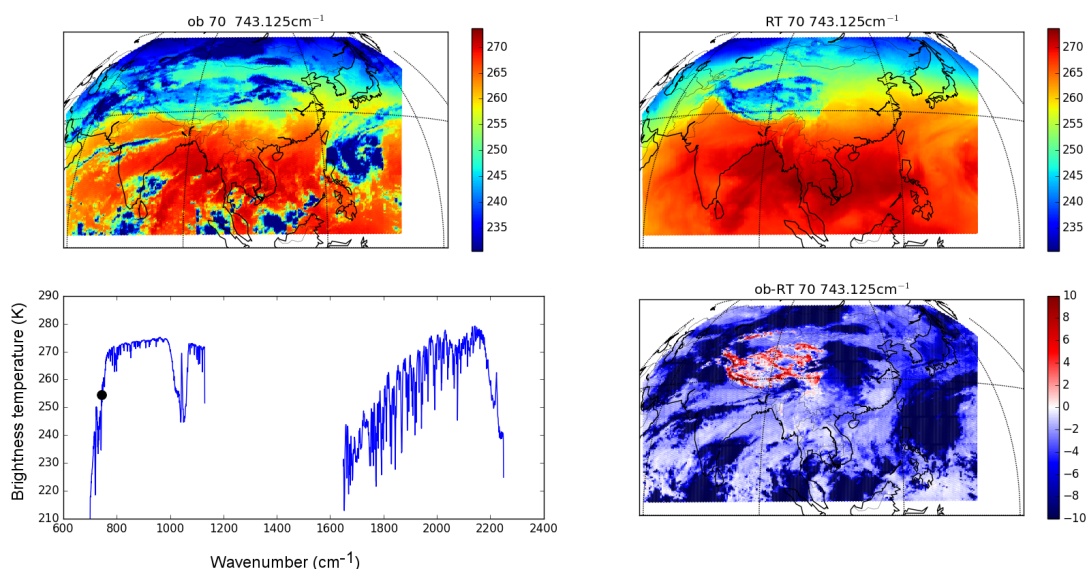


Figure 6: Brightness temperature observations from a single scan of GIIRS channel 70 (743.125cm^{-1}), top left; clear sky model simulations for this scene, top right; a sample brightness temperature spectrum indicating this channel (black circle), bottom left; observation minus simulations, bottom right.

Figures 7 and 8 show similar analyses for two channels in the MWIR band. Figure 7 is for a channel directly on a water vapour absorption line, and Figure 8 is for a neighbouring channel which is off the absorption line. Clearly, the observations on the absorption line exhibit a very large amount of both random and systematic noise, whereas the observations off the line have much better qualitative agreement with the model simulations in the absence of cloud. The observations which are directly on the absorption line represent thermal emission from water vapour relatively high in the tropopause, and hence the low temperature leads to a small measured radiance and so the signal-to-noise ratio is much worse than for the warmer, lower-peaking channels. This limits the useful vertical range of water vapour information that GIIRS can provide.

Note that even in the lower peaking channel (Figure 8), there are some systematic spatial discontinuities across the domain which are seen most clearly in the lower right panel.

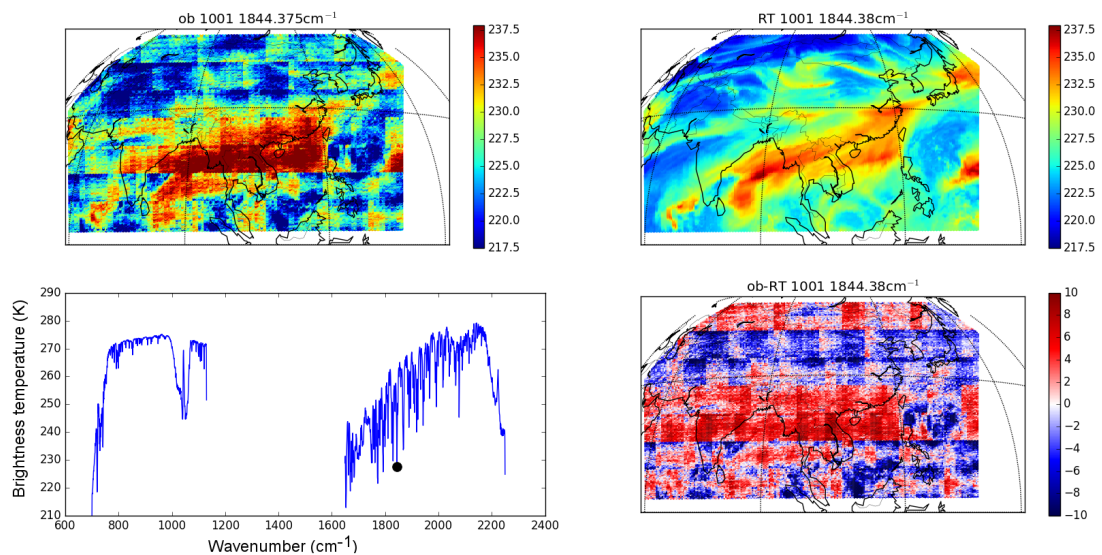


Figure 7: Brightness temperature observations from a single scan of GIIRS channel 1001 (1844.375cm^{-1}), top left; clear sky model simulations for this scene, top right; a sample brightness temperature spectrum indicating this channel (black circle), bottom left; observation minus simulations, bottom right.

As mentioned in Section 1, the GIIRS domain is scanned using a detector with 128 pixels in a 4×32 arrangement, and this array scans the region of Asia in 7 rows of 59 dwells. Figure 3 shows the numbering of the pixels within the detector array, with 4 north-south columns of 32 detectors¹.

As well as direct comparisons between individual GIIRS scans and the model simulations, statistics can be generated for clear sky regions. The cloud detection that is performed is based on the McNally & Watts scheme McNally and Watts (2003), and the choice of LWIR channels used to identify cloud is similar to those used operationally for CrIS, but the “contaminated” part of the LWIR band is not used for GIIRS (i.e. channels 37 to 66 are excluded).

Figure 9 shows the mean O-B (observation minus model background) for each pixel and channel. This shows several features, and should be interpreted in the context of the detector array layout in Figure 3.

¹The LWIR and MWIR pixels are in fact slightly offset from each other — in the model simulations, the geolocation of the LWIR pixels is used in the simulations of both bands

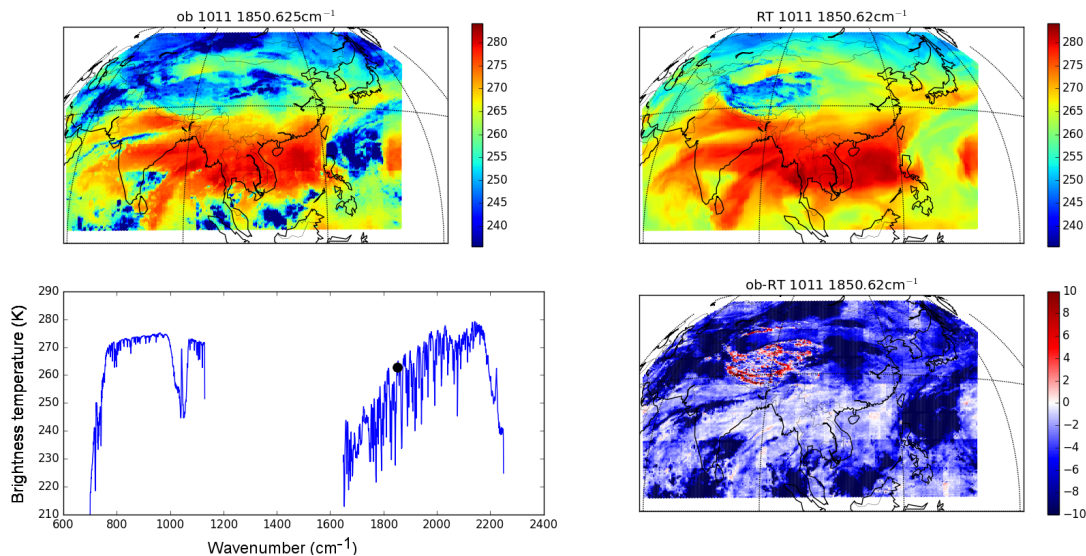


Figure 8: Brightness temperature observations from a single scan of GIIRS channel 1011 (1850.625cm^{-1}), top left; clear sky model simulations for this scene, top right; a sample brightness temperature spectrum indicating this channel (black circle), bottom left; observation minus simulations, bottom right.

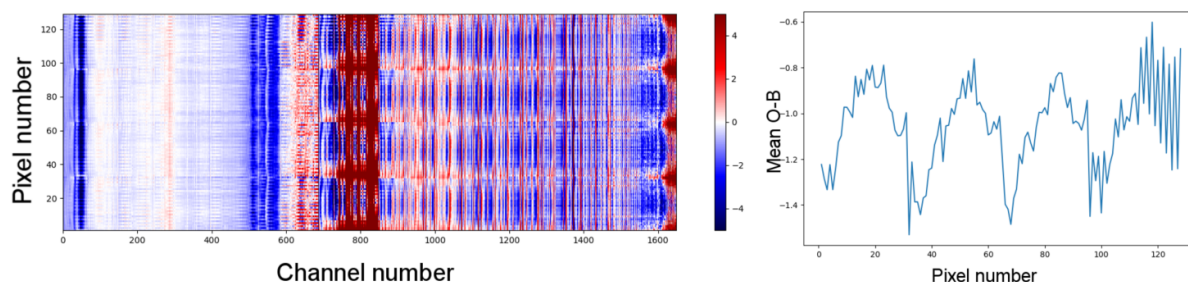


Figure 9: Mean observation minus background for clear sky scenes, for each channel and pixel (left). Mean observation minus background for clear sky scenes, calculated for channel 6 (703.125cm^{-1}) for each pixel (right).

First, note that LWIR covers channels 1-689 and MWIR covers 690-1650 (see Figure 1 for the wavenumbers). The “contaminated” band around channels 37-66 can be seen for all detectors, as can the contaminated spectral region of the MWIR band up to around channel 850. The remainder of the LWIR band looks reasonably consistent with the model on first inspection although there is increased noise at the upper frequency band edge. The remainder of the MWIR band shows strong variation on and off the absorption lines, which can be interpreted in conjunction with Figures 7 and 8, and in general, this indicates that the bias structure is generally smaller and more consistent in the LWIR band compared to the MWIR band.

Now, looking at the variation between the pixels, it can be seen that there are four groups of pixels with consistent-looking characteristics. These repeat every 32 pixels and so each of these bands represents a north-south column in the detector array (c.f. Figure 3). This could be evidence of a residual radiometric calibration error.

Furthermore, in addition to these broad north-south variations across the detector array, there also appears to be a variation in the bias affecting alternating pixels. This is most consistent in LWIR, but is also present in some of the “cleaner” MWIR channels.

Both of these features can be seen when a slice through this graph is plotted for a single channel. This is shown in Figure 9 for channel 6 (703.125cm^{-1}). The broad variability from the north to south of the detector array can be seen for the four sets of 32 pixels, and the difference in bias characteristics for alternating pixels can also be seen, particularly for the column of pixels numbered 97-128.

If we look at the statistics plotted for each pixel, this time for channel 51 (which is known to be “contaminated”), we can see this pattern very clearly, i.e. in Figure 10.

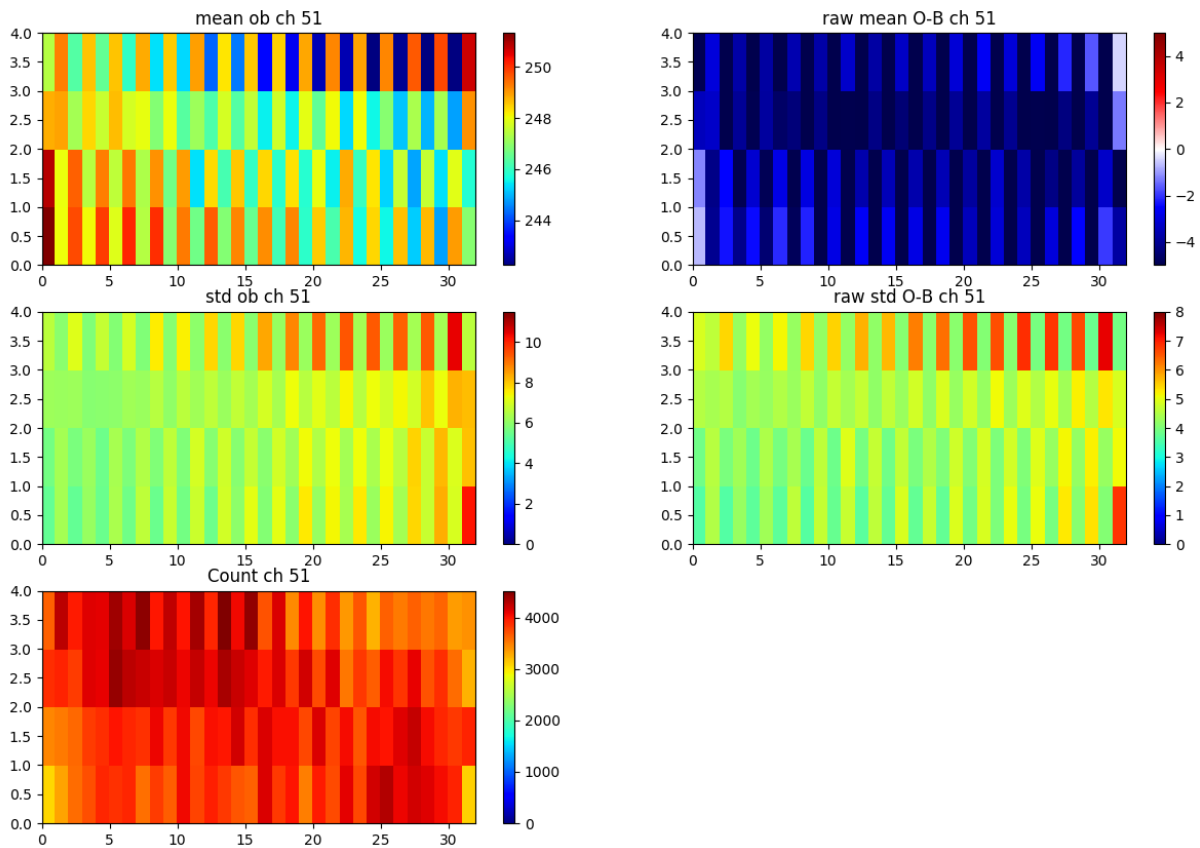


Figure 10: Statistics of observations and O-B for each pixel, for channel 51 (731.25cm^{-1}). The top row shows the mean observed brightness temperature and the mean observation minus simulation. The middle row shows the standard deviations of these quantities and the bottom row shows the number of observations which contributed to the sample.

In Figure 10 the detector array has been rotated 90° anticlockwise. The key things to note are that both the mean and standard deviation vary across the array in similar ways. It appears that the “phase” of the north-south alternating pattern is consistent between the first and second pair of pixel columns as well as the between the third and fourth columns, however the phase is opposite between the two sets of pairs. For a given column of pixels, the bias characteristics of the odd-numbered pixels are generally consistent, as well as between the even-numbered pixels. There are also systematic differences between the columns, and the fourth column is generally much noisier than the other two. Most other channels do not display these characteristics as strongly, but they are reported here as clear evidence of systematic

errors.

Another systematic error that has been diagnosed with NWP fields is the discontinuity of bias characteristics from dwell to dwell. This can be seen in the observations alone for some channels, but O-Bs show this more clearly. The effect is seen in the top panel of Figure 11 for GIIRS channel 34 (720.625cm^{-1}). There are many instances of discontinuities, but prominent examples are over China, where the discontinuities occur in the east-west direction, and also over India, where the discontinuities are in the north-south direction. If the issue was due to calibration, it would be anticipated that the biases across each zonal scan would be uniform as the calibration is performed at the end of each scan. However, the biases show variability zonally. Furthermore, each scan of the GIIRS domain shows a different pattern of spatial discontinuities, so it cannot be attributed to the viewing geometry, and hence a fixed bias correction for each dwell position cannot be applied.

Following on from the considerations of the straylight leakage of radiation between pixels, we can hypothesise that to first order, there may be a bias affecting all pixels within each dwell that is related to the total radiance incident on the dwell. This can be investigated by assessing whether the mean measured signal across the dwell is correlated with the O-Bs of each pixel.² A histogram demonstrating this is shown in Figure 12. Strictly, this analysis should be performed in radiance units, but in this spectral region the Planck function behaves linearly, so using BT units should not be an issue.

Although this channel clearly shows an approximately linear relationship between the O-Bs and the mean BT in each dwell, some other channels do not show such clear behaviour, and for the limited sample used here, the histogram can be bi-modal (not shown). Continuing with this channel, we can attempt to use the linear regression as a bias correction function, where the predictor is the mean BT across each dwell. This bias correction would then be applied to all measurements within that dwell.

At this stage it is important to note that it would be preferable for the correction to be performed as part of the level-1 processing, but this analysis is intended to highlight the way the problem manifests itself, and possibly to be a pre-assimilation bias correction step.

The effect of applying this bias correction for channel 34 is shown in the bottom pair of plots in Figure 11. Compared to the plots of uncorrected values, the discontinuities are substantially reduced. Again, consider the east-west discontinuities over China and the north-south discontinuities over India. In spite of the correction, it can be seen that there are residual systematic biases, particularly variation in the north/south direction across the detector array. Further investigation is required to determine if this is due to a deficiency in this approach or whether there is an additional contributory effect such as a residual spectral calibration error. The correction proposed here is simple in that the mean of the measured BT across the detector array is used as a predictor, but the pixels at the extreme north and south ends of the detector array are likely to receive less leakage radiation than pixels in the centre, so a further refinement could be made.

3.2 Diurnal variations

For data assimilation, the issue of diurnal biases is both important and difficult. It is difficult because the models themselves can exhibit diurnal biases, as can the observations themselves, mostly because of solar effects on in situ or remote sensing instruments. For three-axis-stabilised geostationary satellites, the sun illuminates the spacecraft differently depending on the time of day (and this changes throughout the year). Therefore, radiometric contributions from radiative heating of the instrument can vary diurnally.

²Note that nonlinearity of instrument calibration could also lead to a similar correlation.

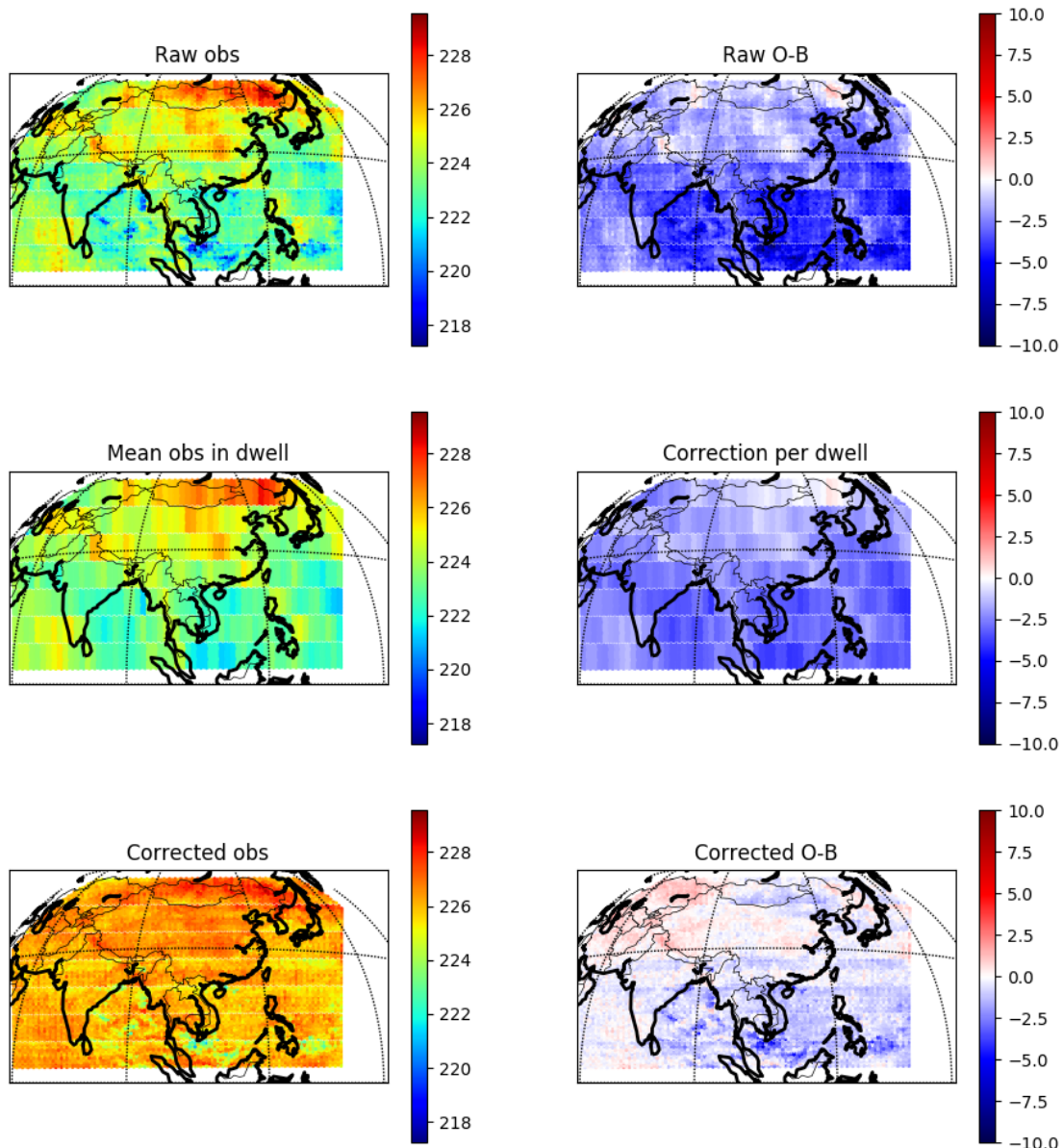


Figure 11: The top pair of plots show the mean of the observations in BT units (left) and O-Bs (right) for channel 34 (720.625cm^{-1}). The middle pair of panels shows the mean observation and O-B across each dwell, and the bottom pair shows the mean observations and O-Bs when the correction has been applied.

The mean O-B for GIIRS channel 33 (720.0cm^{-1}) is shown in Figure 13, where the statistics have been binned for different UTC hours. It can be seen that a gap is present at around 17UTC because each day, no data are provided for this period due to solar intrusions close to local midnight. Despite this, just prior to the outage, the bias for this channel increases greatly, so usage of data should be restricted to avoid this large bias.

Otherwise, there is a smooth diurnal variation in the O-Bs which is visible, however, it is not straightforward to discern whether this is due to the observations themselves or the NWP model.

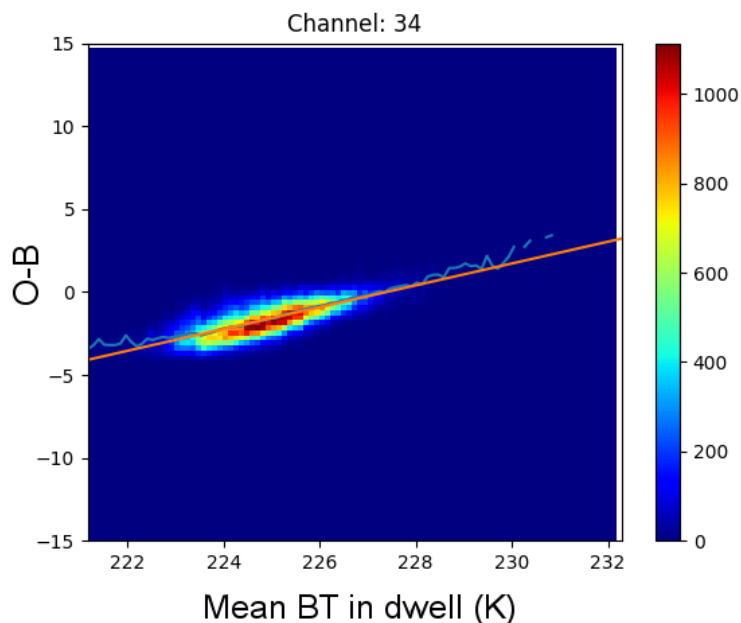


Figure 12: Histogram of O-Bs against the mean across each dwell for channel 34 (720.625cm^{-1}). The linear regression is shown in orange.

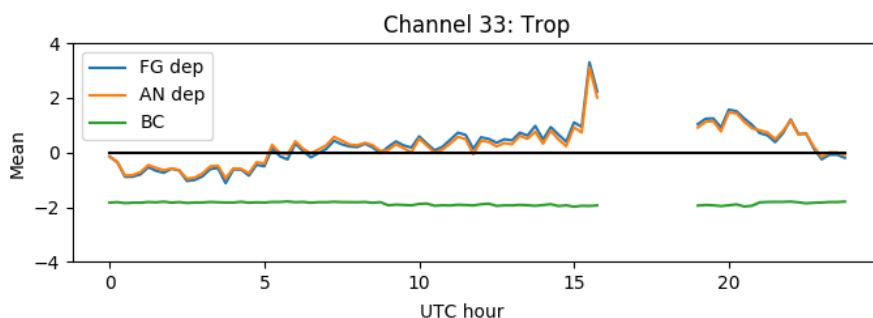


Figure 13: Mean O-B (and O-A) for GIIRS channel 33 (720.0cm^{-1}) binned by UTC hour.

4 Preliminary GIIRS assimilation trials

Preparing an NWP system for the assimilation of data from GIIRS requires many of the same considerations as would be needed for a hyperspectral infrared instrument on a LEO platform, but with some further specific considerations.

4.1 Channel selection

It is too computationally costly to assimilate all channels of a hyperspectral sounder, so a subset of channels is used. This also enables the exclusion of channels which are known to exhibit large noise, or systematic deficiencies. The selection of 72 channels used here is as follows: 2, 3, 4, 5, 6, 7, 8, 11, 12, 13, 14, 15, 16, 17, 19, 21, 25, 26, 27, 28, 29, 30, 31, 33, 34, 35, 36, 67, 93, 97, 101, 105, 115, 130, 237, 269, 329, 377, 510, 514, 518, 522, 526, 530, 534, 538, 542, 546, 565, 569, 573, 577, 581, 585, 985, 994,

1011, 1018, 1030, 1055, 1069, 1091, 1099, 1111, 1139, 1174, 1191, 1209, 1216, 1223, 1245, 1251.

Channel	Band	Wavenumber (cm^{-1})	Wavelength (micron)	Weighting function peak (hPa)	Sensitivity
2	1	700.625	14.27	29	Temp

Where possible, this matches the channel selection which is used operationally at ECMWF for CrIS (the spectral sampling and resolution is the same in LWIR). Between channels 36 and 67 in the LW band, no channels are used because these exhibit large noise and have been described as “contaminated”. Furthermore, many of the higher-peaking water vapour channels in the MW band exhibit large noise and systematic discontinuities between dwells, so these are excluded, and the selected channels are those which do not lie on the water vapour absorption lines.

An objective selection of channels (to maximise information content) has not been performed here, and the selection presented here is subject to further refinement.

4.2 Pixel selection

In order to maintain a sample with consistent statistics, a pixel selection has been determined which includes alternate pixels from the array. The numbers of these pixels are 3, 5, 7, 9, 11, 13, 15, 17, 19, 21, 23, 25, 27, 29, 68, 70, 72, 74, 76, 78, 80, 82, 84, 86, 88, 90, 92, 94 (cf. Figure 3). As well as providing consistent data characteristics, using this subset of observations effectively thins the data to useable volumes. A further refinement would be to dynamically perform the thinning to improve the coverage of cloud-free scenes in the sample to be assimilated.

4.3 Observation errors

A critical aspect of the assimilation of any observation is the prescription of an appropriate estimate of the observation error (i.e. statistical uncertainty). This enables the model state to be pulled towards the observations commensurately with the respective errors of the observations and the initial state of the model. The observation uncertainties can be estimated using several techniques, each of which has their own limitations. A popular method is that proposed by Desroziers (Desroziers et al. (2005)), which was intended as a consistency-check of the prescribed errors, but can also be used to estimate the observation errors using statistics of O-B and O-A in an assimilation system which has already ingested the observations.

A benefit of the Desroziers method is that it can produce full observation error covariance matrices. The ECMWF global model (IFS) is set up to make use of inter-channel observation error correlations (Bormann et al. (2016)), and so such matrices (denoted \mathbf{R}) are diagnosed and used in this study.

The result of the Desroziers method is not necessarily invertible, nor is it even guaranteed to be symmetrical. Therefore a series of steps are applied to process the matrix into a useable and numerically well-behaved form:

1. Make the matrix symmetrical: $\mathbf{R} = 0.5(\mathbf{R}_{init} + \mathbf{R}_{init}^T)$.
2. Perform an eigenvalue decomposition and set a lower floor on the eigenvalues so as to improve the condition number of the matrix.

3. The resulting matrix is then split into its correlation matrix and variance values. Any correlations outside the range $-1 \geq \text{corr} \geq 1$ are clipped.
4. The covariance matrix is reconstructed.

The correlation matrix after step 1 had been applied is shown in Figure 14 and the corresponding uncertainty standard deviations are shown in Figure 15. The correlation matrix is qualitatively similar to that diagnosed for CrIS (Eresmaa et al. (2017)) and shows clear blocks of similar channels; LW temperature, window, ozone and water vapour as the channel number increases.

The square root of the variance values show that the smallest errors for this channel selection occur for the high peaking long-wave temperature-sounding channels and the window channels; the largest errors occur for the ozone channels and mid-wave water vapour channels.

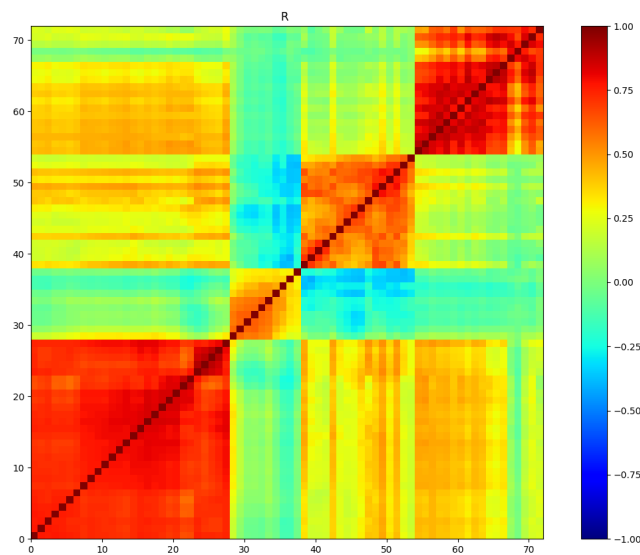


Figure 14: Observation error correlation matrix for GIIRS as diagnosed by the Desroziers method. The channel indices refer to the subset noted in Section 4.1.

As mentioned above, the observation error covariance matrix produced by the Desroziers technique can be numerically unstable on inversion. To ameliorate this, we can impose certain restrictions on the eigenvalues of the matrix. Firstly, the “condition number”, κ is defined as the ratio of the maximum and minimum eigenvalues of the matrix:

$$\kappa(\mathbf{R}) = \frac{|\lambda_{\max}(\mathbf{R})|}{|\lambda_{\min}(\mathbf{R})|}$$

The larger the condition number is, the less numerically stable it is. The method of *reconditioning* the matrix used here allows a required condition number to be obtained by manipulating the values in the matrix. To achieve this, given the largest eigenvalue of the matrix, we can determine the smallest eigenvalue that will satisfy the constraint on the condition number. Therefore, any of the eigenvalues that are smaller than this value are set to be equal to this value. Figure 16 shows the correlation matrices and standard deviations of the diagnosed \mathbf{R} matrix for a range of condition numbers.

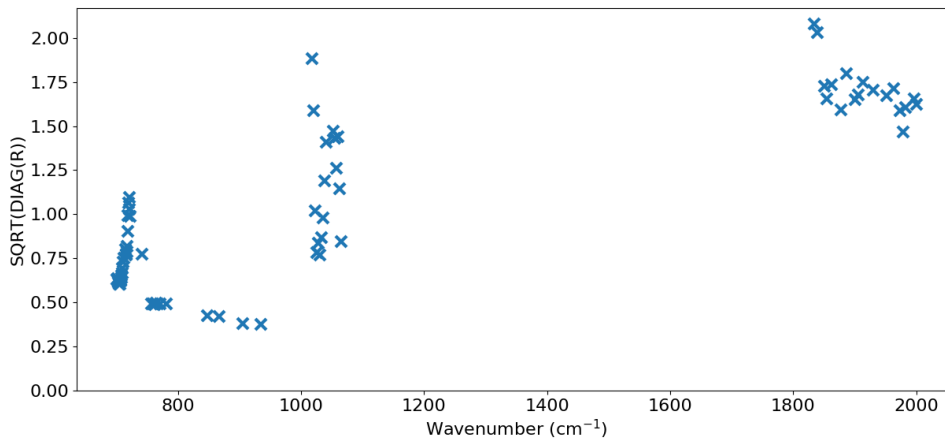


Figure 15: Square root of the diagonal of the diagnosed GIIRS covariance matrix (i.e. brightness temperature standard deviations in units of Kelvin).

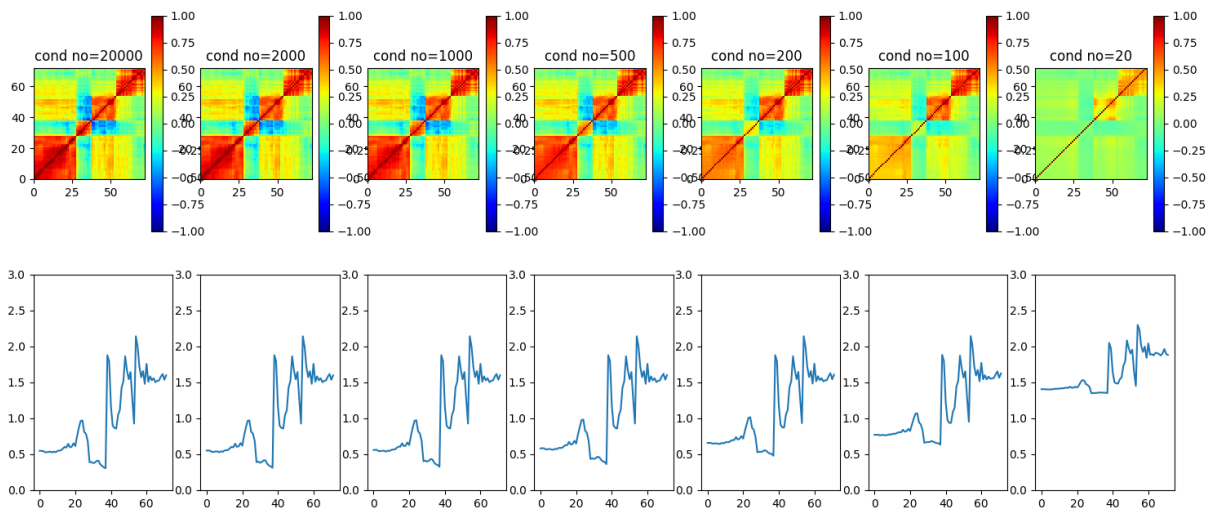


Figure 16: GIIRS observation error correlation matrix and the square root of the diagonal of \mathbf{R} for a range of prescribed condition numbers.

The clear trend is that the closer the condition number is to unity, the more diagonal the correlation matrix becomes and the larger the standard deviations become. Therefore, a compromise must be reached between the assumed accuracy of the original matrix, and the numerical stability introduced by the reconditioning. Without any reconditioning, the 4D-Var assimilation system fails to converge altogether, so some level of reconditioning is certainly required. For the purposes of this study, the condition number of 500 has been selected.

4.4 Cloud detection and bias correction

If a cloud enters an otherwise cloud-free scene, the change in brightness temperature observed by a remote sensing IR instrument can exceed 50K. Currently at ECMWF, the assimilation of radiance data

cannot handle cloudy scenes fully. So it is vital to ensure that in the presence of cloud, only those channels which are not significantly affected by the atmosphere at the height of the cloud are assimilated to avoid producing large detrimental increments to the analysis. The algorithm to perform this cloud detection was developed by McNally and Watts (McNally and Watts (2003)).

Another aspect which is important to comply with the basic assumptions of data assimilation is that the observations are unbiased. To address this, most passive radiance observations are bias-corrected prior to being assimilated, and in fact at ECMWF, the bias correction is adapted automatically from day to day within the 4D-Var system itself. This is known as variational bias correction or VarBC (Dee and Uppala (2009)).

These two aspects of cloud detection and bias correction are both vital, but we encounter a problem when we ingest new observations into the assimilation system for the first time, and this is particularly problematic for geostationary radiances. The problem is that before a bias correction has been computed, the cloud detection will misidentify clear and cloudy scenes because the observations are potentially biased to begin with. Furthermore, the bias corrections cannot be calculated accurately because the cloud detection is not able to identify clear scenes well enough. Therefore, this cyclical loop needs to be broken. The procedure proposed here is as follows.

1. First, a clean window channel is selected. In this case, channel 278 (873.125cm^{-1}).
2. The O-Bs for this channel are assessed for a large sample of GIIRS data. Note that the model simulations do *not* include cloud.
3. A histogram of O-Bs will show clear asymmetry, with many more observations being colder than the simulations compared to the converse. It is proposed that the mode of the first guess departures for this channel is not strongly sensitive to cloud because the warm side of the histogram is approximately Gaussian. This mode is taken to be an estimate of the bias of the observations for this channel.
4. Observations for this channel are bias-corrected using this estimate.
5. A sample of spectra is obtained by applying the stringent constraint that over ocean, for this window channel, $|O - B| < 0.5K$. This sample is assumed to be fully cloud-free.
6. For each of the channels in this sample a histogram of O-Bs is produced, and a Gaussian function is fitted to it. The mean of this Gaussian function is taken to be in the initial estimate of the bias in the channel, and the fitting of the Gaussian enables this to be a robust statistic.
7. These bias corrections are used in the assimilation from the start, but the additional air-mass bias predictors are permitted to evolve from this starting point.

In Figure 17, this method has been applied for a MWIR water vapour channel. The sample in the right panel has been selected using the window channel check described above, and the mean of the fitted Gaussian is the initial estimate of the bias correction.

Although most GIIRS channels are processed in the VarBC framework, a single ozone channel (542, i.e. 1038.125cm^{-1}) is deliberately assimilated without any bias correction in order that the ozone field is “anchored” and hence does not drift due to reinforcing biases from similar channels.

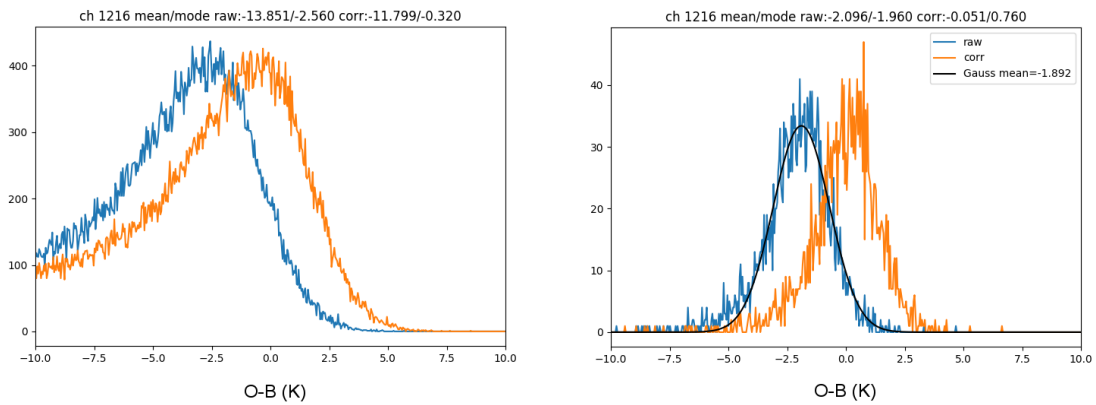
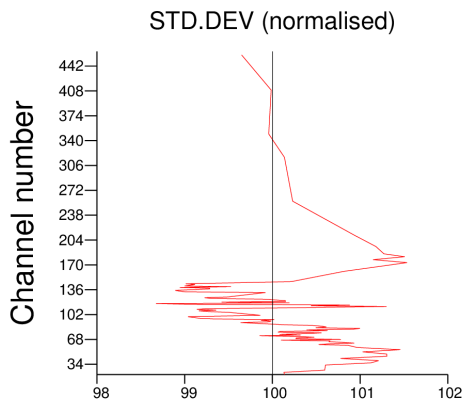


Figure 17: O-B histograms for a water vapour channel. The left panel shows the histogram of the entire sample (i.e. including cloud-affected scenes) in blue and the right panel shows the histogram of those which are determined to be cloud-free in blue. The fitted Gaussian is shown in black, and the orange lines show the histograms after the bias correction has been applied.

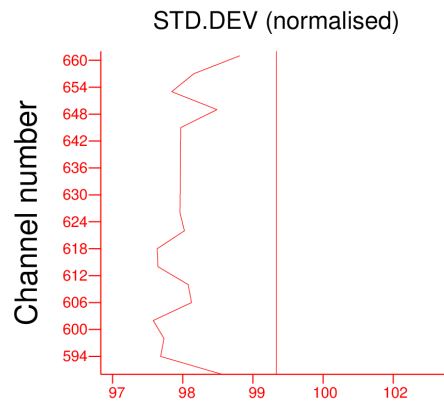
4.5 Forecast impact

Figures 18 and 19 show the change in the standard deviation of CrIS O-Bs calculated over the GIIRS domain when GIIRS observations are assimilated. Values below 100% indicate that when GIIRS is assimilated, the short range forecasts are closer to the independent CrIS observations. By inflating the observation errors by a factor of 3 (Figure 19), the fits are generally better than with no inflation applied.

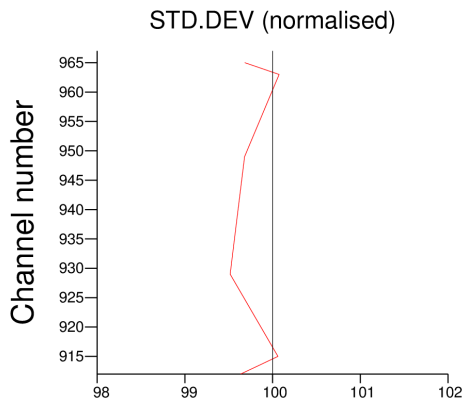
2020100100-2020101012(12)
 CRIS areaNSEW= 50/ 0/ 150/ 50
 used Tb (LW : from 1 to 547)



2020100100-2020101012(12)
 CRIS areaNSEW= 50/ 0/ 150/ 50
 used Tb (O3 : from 549 to 661)



2020100100-2020101012(12)
 CRIS areaNSEW= 50/ 0/ 150/ 50
 used Tb (WV : from 705 to 975)



2020100100-2020101012(12)
 CRIS areaNSEW= 50/ 0/ 150/ 50
 used Tb (SW : from 978 to 1109)

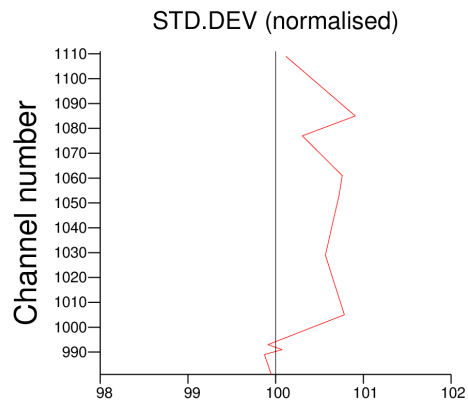
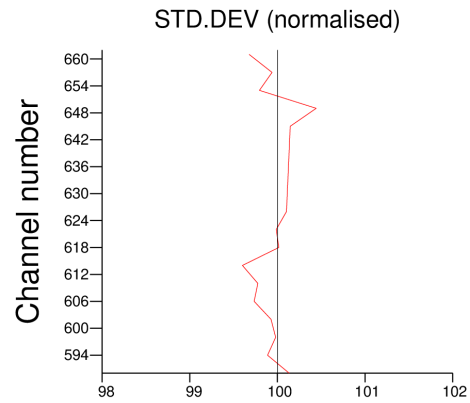
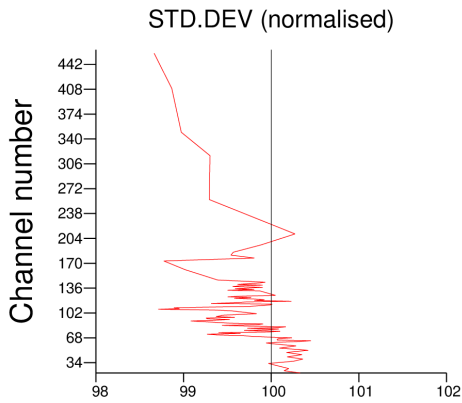


Figure 18: Normalised change in the standard deviation of CrIS O-Bs calculated over the GIIRS domain (values smaller than 100% indicate an improvement). The change is the effect of assimilating GIIRS. The observation errors are unscaled.

2020100100-2020101012(12)
 CRIS areaNSEW= 50/ 0/ 150/ 50
 used Tb (LW : from 1 to 547)

2020100100-2020101012(12)
 CRIS areaNSEW= 50/ 0/ 150/ 50
 used Tb (O3 : from 549 to 661)



2020100100-2020101012(12)
 CRIS areaNSEW= 50/ 0/ 150/ 50
 used Tb (WV : from 705 to 975)

2020100100-2020101012(12)
 CRIS areaNSEW= 50/ 0/ 150/ 50
 used Tb (SW : from 978 to 1109)

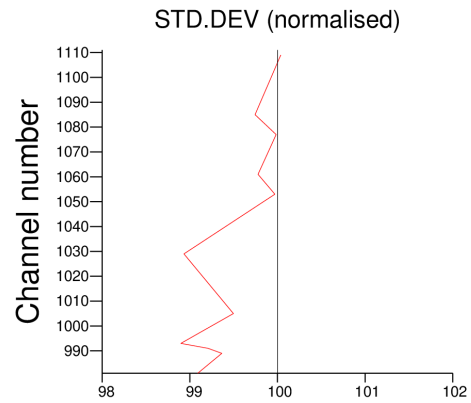
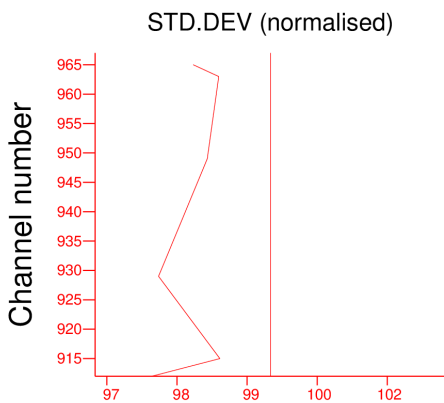


Figure 19: Normalised change in the standard deviation of CrIS O-Bs calculated over the GIIRS domain (values smaller than 100% indicate an improvement). The change is the effect of assimilating GIIRS. The observation errors are scaled by a factor of 3.

5 Summary

The GIIRS instrument onboard FY-4A is the first hyperspectral infrared sounder on a geostationary platform, and the analysis performed here has highlighted a number of systematic features in the GIIRS observations, although it should be noted that subsequent instruments (including GIIRS on FY-4B are anticipated to have fewer deficiencies). Comparisons with collocated IASI observations have indicated that the spectral calibration of GIIRS varies across the detector array, with a range as large as 30ppm in the LWIR band. IASI has also been used to assess the radiometric characteristics of GIIRS, and has indicated a scene-dependence, whereby scenes with different amounts of cloud can have biases compared to IASI of 1 to 2 K.

Straylight is the phenomenon where internal reflections/scattering within the instrument result in the detector array having a broad point spread function. This has been investigated by looking at the sharp interface of the Earth's limb, and it has been shown that as more of the detector array is measuring terrestrial radiation, the pixels in the array measuring space show an increase in signal from the straylight.

To complement the IASI collocation investigations, analyses have also been performed to compare GIIRS observations with radiance simulations from short range model forecasts (i.e. "backgrounds"). This has highlighted a number of systematic features in the GIIRS data. Notably, for several spectral regions, there are significant steps in the bias between fields of regard. This varies from scan to scan, and is particularly problematic in the higher peaking water vapour channels. Assuming that this is somehow related to the straylight issue, a correction has been proposed. This correction does not work well for all channels, so it is not expected to be used in practice, but it may be helpful for informing decisions regarding future instrument design. Also, an alternating bias pattern across the detector array has been noticed, and shown here for a contaminated region of the LWIR band. Finally, a diurnal signal was identified, although it is unclear how much, if any, of this signal is coming from the observations. However, just before the daily outage to prevent solar contamination, there appears to be a spike in the time series, so it may be advisable not to use data from the last scan before the outage.

Assimilation experiments have been performed using GIIRS observations. The setup has been described, including the channel selection, pixel selection, observation errors (including details of how they were generated). The solution to the intertwined issue of bias correction and cloud detection of new observations has been explored and a method has been proposed to overcome this. The results of the assimilation experiments show modest improvements in the fits of the short range forecasts to independent observations close to the GIIRS domain, however, greater impact can be expected from improved instruments in the future and refined assimilation methodology.

6 Acknowledgements

Several people have contributed directly or indirectly to this project. Many thanks to Tony McNally, Dorothee Coppens, Bertrand Theodore, Thomas August, Peter Lean, Qiang Guo and Sylvain Abdon.

7 Annex: Pre-agreed aims and division of responsibility of the collaborative study

The main interests of the joint study were to:

- develop the quality analysis capabilities of both teams on unknown data, in particular EUMETSAT is developing right now the future monitoring routines of IRS,
- analyse the GIIRS data quality in order to integrate the GIIRS instrument into the cross-calibrations performed regularly between all infrared sounders as IASI (on-board Metop-C), CrIS (Suomi NPP) or HIRAS (FY-3),
- learn how to assimilate IRS-like observations in a global NWP model and to evaluate with real proxy-data the potential impact of MTG-S IRS for this application.

In addition, the main challenges were to:

- analyse the data quality without any engineering data or previous on-ground characterisation,
- prepare an assimilation experiment of highly resolved spectral information at such a high spatio-temporal density, a combination never met before. The only possible experiments of assimilating IRS-like measurements so far were performed with simulated data, in so-called Observing System Simulation Experiments (OSSE) (Errico et al. (2013)).

Both teams worked on their main interests as follow:

- EUMETSAT focused on spatio-temporal collocations between GIIRS and IASI measurements, the latter taken as a reference. It leads to very precise comparison since the atmospheric states of the measurements are the same but the geolocations and time statistics are limited.
- ECMWF focused on comparison between the GIIRS measurements and RT (radiative transfer) models using forecast information. It allows large statistical samples but the comparisons are only valid in clear sky conditions (since clouds are very challenging to model).

References

- Bormann, N., Bonavita, M., Dragani, R., Eresmaa, R., Matricardi, M., and McNally, A.: Enhancing the impact of IASI observations through an updated observation-error covariance matrix, *Quarterly Journal of the Royal Meteorological Society*, 142, 1767–1780, <https://doi.org/https://doi.org/10.1002/qj.2774>, URL <https://rmets.onlinelibrary.wiley.com/doi/abs/10.1002/qj.2774>, 2016.
- Burrows, C.: Assimilation of radiance observations from geostationary satellites: third year report, <https://doi.org/10.21957/spbzz81e3>, URL <https://www.ecmwf.int/node/19483>, 2020.
- Dee, D. P. and Uppala, S.: Variational bias correction of satellite radiance data in the ERA-Interim reanalysis, *Quarterly Journal of the Royal Meteorological Society*, 135, 1830–1841, <https://doi.org/https://doi.org/10.1002/qj.493>, URL <https://rmets.onlinelibrary.wiley.com/doi/abs/10.1002/qj.493>, 2009.
- Desroziers, G., Berre, L., Chapnik, B., and Poli, P.: Diagnosis of observation, background and analysis-error statistics in observation space, *Quarterly Journal of the Royal Meteorological Society*, 131, 3385–3396, <https://doi.org/https://doi.org/10.1256/qj.05.108>, URL <https://rmets.onlinelibrary.wiley.com/doi/abs/10.1256/qj.05.108>, 2005.
- Eresmaa, R., Letertre-Danczak, J., Lupu, C., Bormann, N., and McNally, A. P.: The assimilation of Cross-track Infrared Sounder radiances at ECMWF, *Quarterly Journal of the Royal Meteorological Society*, 143, 3177–3188, <https://doi.org/https://doi.org/10.1002/qj.3171>, URL <https://rmets.onlinelibrary.wiley.com/doi/abs/10.1002/qj.3171>, 2017.

Errico, R. M., Yang, R., Privé, N. C., Tai, K.-S., Todling, R., Sienkiewicz, M. E., and Guo, J.: Development and validation of observing-system simulation experiments at NASA's Global Modeling and Assimilation Office, *Quarterly Journal of the Royal Meteorological Society*, 139, 1162–1178, <https://doi.org/https://doi.org/10.1002/qj.2027>, URL <https://rmets.onlinelibrary.wiley.com/doi/abs/10.1002/qj.2027>, 2013.

Guo, Q., Chen, B., Wang, X., Han, C., Hui, W., Xu, W., and Wen, R.: Spectrum Calibration of the First Hyperspectral Infrared Measurements from a Geostationary Platform: Method and Preliminary Assessment, *Quarterly Journal of the Royal Meteorological Society*, 147, <https://doi.org/10.1002/qj.3981>, 2021.

McNally, A. P. and Watts, P. D.: A cloud detection algorithm for high-spectral-resolution infrared sounders, *Quarterly Journal of the Royal Meteorological Society*, 129, 3411–3423, <https://doi.org/https://doi.org/10.1256/qj.02.208>, URL <https://rmets.onlinelibrary.wiley.com/doi/abs/10.1256/qj.02.208>, 2003.